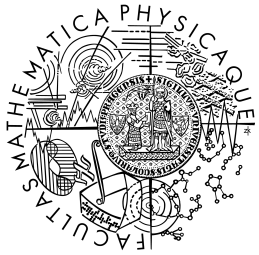

FACULTY
OF MATHEMATICS
AND PHYSICS
Charles University

Summary of doctoral thesis

Ľubica Valentová

Three-dimensional ambient noise tomography of the Bohemian Massif

Department of Geophysics

Supervisor of the doctoral thesis:	Doc. RNDr. František Gallovič, Ph.D.
Study programme:	Physics
Study branch:	Geophysics

Prague 2017

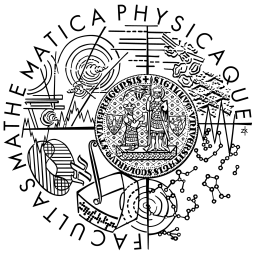

MATEMATICKO-FYZIKÁLNÍ
FAKULTA
Univerzita Karlova

Autoreferát dizertační práce

Ľubica Valentová

Trojrozměrná tomografie Českého masivu ze seismického šumu

Katedra geofyziky

Vedoucí disertační práce:	Doc. RNDr. František Gallovič, Ph.D.
Studijní program:	Fyzika
Studijní obor:	Geofyzika

Praha 2017

Dizertace byla vypracována na základě výsledků získaných v letech 2009–2017 během doktorandského studia na Katedre geofyziky MFF UK a vrámci projektu QUEST na KAFZM, FMFI UK v Bratislavě.

Dizertant:
Mgr. Ľubica Valentová
Katedra geofyziky MFF UK
V Holešovičkách 2, 180 00 Praha 8

Školitel:
Doc. RNDr. František Gallovič, Ph.D.
Katedra geofyziky MFF UK
V Holešovičkách 2, 180 00 Praha 8

Oponenti:
RNDr. Jan Burjánek, Ph.D.
Geofyzikální ústav Akademie věd, v. v. i.
Boční II/1401, 141 31 Praha 4

Doc. Mgr. Jozef Kristek, Ph.D
Katedra astronómie, fyziky Zeme a meteorológie FMFI UK
Mlynská dolina F1, 842 48 Bratislava, Slovenská republika

Předsedkyně oborové rady:
Doc. RNDr. Hana Čížková, Ph.D.
Katedra geofyziky MFF UK
V Holešovičkách 2, 180 00 Praha 8

Obhajoba dizertace se koná dne 26. 4. 2018 v 13:00 hodin před komisí pro obhajoby dizertačních prací v oboru Geofyzika v budově MFF UK, Ke Karlovu 3, Praha 2 v místnosti M252.

S dizertací je možno se seznámit v PGS MFF UK, Ke Karlovu 3, Praha 2.

Contents

Introduction

We have performed 3D ambient noise tomography of the Bohemian Massif. We invert adopted inter-station dispersion curves of both Love and Rayleigh waves in periods 4–20 s, which were extracted from ambient noise cross-correlations by Růžek et al. (2016), using a two-step approach. In the first step, the inter-station dispersion curves are localized for each period into the so-called dispersion maps. To account for finite-frequency effects, gradient method employing Fréchet kernels is used. Assuming membrane wave approximation of the surface wave propagation at each period, the kernels were calculated using the adjoint method (Tromp et al. (2005); Fichtner et al. (2006)). To reduce the effect of data noise, the kernels were regularized by Gaussian smoothing. The proper level of regularization is assessed on synthetic tests. In the second step, the phase-velocity dispersion maps are inverted into a 3D S-wave velocity model using Bayesian approach (Tarantola (2005)). The posterior probability density function describing the solution is sampled by more than one million models obtained by Monte-Carlo approach, in particular parallel tempering algorithm (Sambridge (2014)). The calculated variance of the model shows that the well resolved part corresponds to the upper crust (i.e., upper 20 km). The mean velocity model contains mainly large scale structures that show good correlation with the main geologic domains of the Bohemian Massif. Furthermore, in the well-studied area of Western Bohemia our model agrees well with S-wave velocity models published by other authors.

1 Method

1.1 Adjoint tomography

The adjoint method may be viewed as a finite-frequency generalization to traditionally employed ray method as it accounts for the volumetric dependency of wave propagation on seismic properties of media (similar to Fresnel zone in optics) represented by the so-called sensitivity kernels.

Simply put, the objective of the seismic tomography is to minimize the misfit between the synthetics and measurements as function of material parameters. For our application, we assume misfit as L2 norm of cross-correlation traveltime residuals:

$$\chi = \frac{1}{2}\sum_i h_i \Delta T_i^2. \tag{1}$$

where the traveltime residual ΔT_i between the synthetic seismogram u_i and observed seismogram u_i^0 is given as the time of their cross-correlation maximum:

$$\Delta T_i = \arg\max_t \int u_i(\tau) u_i^0(t+\tau) d\tau. \tag{2}$$

Moreover, the synthetic wavefield u_i satisfies condition of membrane wave propagation for all $\mathbf{x}$ and t

$$\rho(\mathbf{x})\ddot{u}(\mathbf{x},t) - \nabla\cdot\big(\mu(\mathbf{x})\nabla u(\mathbf{x},t)\big) = f(\mathbf{x},t) \tag{3}$$

and corresponding boundary and initial conditions. In further, we assume density ρ to be homogeneous.

To minimize/maximize a functional which is also subject to another contraint(s), the method of Lagrange multiplier is employed (Liu and Tromp (2006)).

It can be shown, that the derivative of the Lagrangian $\mathcal{L}$ with respect to the model parameter $\mu(\mathbf{x})$ can be simplified to

$$\delta_\mu \mathcal{L} = \sum_i \int_\Omega \int_t 2\delta\mu(\nabla\lambda_i(\mathbf{x},t)\cdot\nabla u_i(\mathbf{x},t))\mathrm{d}t\mathrm{d}V, \tag{4}$$

if the Lagrange multipliers λ_i satisfy the so-called adjoint equation, which in case of membrane waves is identical to the original equation of membrane wave, but with adjoint sources (e.g., Luo and Schuster (1991))

$$f_i^\dagger = -\frac{\dot{u_i}}{\int \dot{u_i}^2 dt}\delta(x - x_i). \tag{5}$$

To obtain the derivative of the Lagrangian, two calculations for each measurement i are performed: one forward calculation of the wavefield propagation from source to receiver and one adjoint calculation (in our application this refers to the backward propagation of the wavefield from receiver to the sources). After combining these wavefields into the Lagrangian derivative according to (4), it is used in the minimization procedure using e.g. conjugate gradient method.

Here, the volumetric distribution of the Lagrangian (and also the misfit) derivative is corresponding to the sensitivity kernel

$$K_\mu(\mathbf{x}) = \int_t 2\nabla u(\mathbf{x},t)\cdot\nabla\lambda(\mathbf{x},t)\mathrm{d}t. \tag{6}$$

The sensitivity kernels have several important properties: firstly, they are dependent on the chosen type of misfit. Secondly, they are dependent on the frequency content of the employed data: the higher is the frequency, the narrower is the corresponding sensitivity kernel. Moreover, the sensitivity kernels contain singularities in points of source and receivers (i.e. where the adjoint source is located). In Fig. 1, we show example of cross-correlation traveltime kernel corresponding to 20 s wavefield.

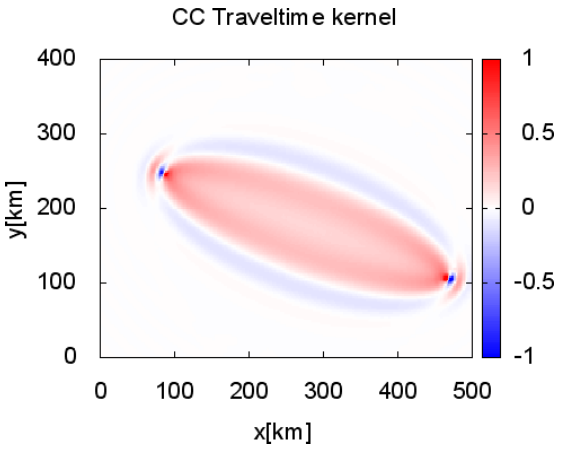

Figure 1: Sensitivity kernels for cross-correlation traveltime misfit using wavefield with 20 s dominant period.

The adjoint method can be derived for arbitrary misfit when the measurements are subject to condition that can be expressed by any linear differential operator.

1.2 Bayesian tomographic inversion

We apply Bayesian approach to solve the second stage of the inverse problem. The result is given by the posterior probability density function (PDF) on model space (e.g., Tarantola (2005)).

The posterior PDF is usually expressed using the Bayes theorem:

$$p(\boldsymbol{m}) = k\ p_{\mathrm{prior}}(\boldsymbol{m})p(\boldsymbol{d}_{\mathrm{obs}}|\boldsymbol{m}) \tag{7}$$

where k is a PDF normalization constant, $p_{\mathrm{prior}}(\boldsymbol{m})$ is prior PDF, $p(\boldsymbol{d}_{\mathrm{obs}}|\boldsymbol{m})$ is the so-called likelihood function. The likelihood function contains statistical information on the data measurement error, but may also include modeling error.

Usually, the data PDF is considered in a form of Gaussian distribution, then

$$p(\boldsymbol{d}_{obs}|\boldsymbol{m}) \propto exp(-S(\boldsymbol{m})), \tag{8}$$

where $S(\boldsymbol{m})$ defines misfit between measured data $\boldsymbol{d}_{\mathrm{obs}}$ and synthetics calculated using a theoretical relation $\boldsymbol{g}(\boldsymbol{m})$ with Gaussian covariance matrix $\mathbf{C}_{\mathrm{d}}$:

$$S(\boldsymbol{m}) = (\boldsymbol{d}_{\mathrm{obs}} - \boldsymbol{g}(\boldsymbol{m}))^T\mathbf{C}_{\mathrm{d}}^{-1}(\boldsymbol{d}_{\mathrm{obs}} - \boldsymbol{g}(\boldsymbol{m})) \tag{9}$$

The result of the inversion is represented by a set of model samples obtained by a random walk according to the posterior PDF. In our application, the data are represented by 2D distribution of dispersion curves. The model is given as 3D S-wave velocity distribution.

To draw samples from the model space according to the posterior PDF, the Markov chain MC random walker is employed. To increase the efficiency of the sampler we apply a method called parallel tempering (PT, Sambridge (2014)). The PT algorithm is similar to the better-known simulated annealing, as it introduces modification of the PDF by an additional parameter called temperature T. The modified PDF $p(\boldsymbol{m}, T)$ is given by

$$p(\boldsymbol{m}, T) = k\ p_{\text{prior}}(\boldsymbol{m}) \exp\left(\frac{-S(\boldsymbol{m})}{T}\right). \tag{10}$$

The samples are drawn following this modified PDF assuming multiple values of the temperature T. The chains with lower temperature values sample locally areas of PDF maxima, whereas chains with higher temperatures (i.e. the PDF is more flat) are able to escape the local maxima of PDF. Moreover, two chains can exchange their temperature values between the chain advances. The PT algorithm is well balanced between efficiency and stability for complex multimodal PDFs (Sambridge (2014)). The method is appropriate for non-linear problems, such as inversion of dispersion curves.

2 Choice of regularization in adjoint tomography based on two-dimensional synthetic tests

The tomographic problem addressed here is based on the 2D adjoint inversion of the 20 s Love-wave traveltimes obtained from the ambient noise cross-correlations across the Czech Republic.

The adjoint method belongs to finite-frequency iterative gradient methods of the misfit minimization. The sensitivity kernels of the misfit gradient are obtained as a combination of the forward and adjoint wavefields. Nevertheless, to avoid artefacts in the resulting model originating in the data noise the method requires regularization, for example, by smoothing of the sensitivity kernels. It should be noted that, besides explicit regularization (e.g., by smoothing of the gradient kernel), the implicit regularization (e.g., number of iteration in the gradient method) is also involved. The regularization setting has an important influence on the resulting model and one must take great care in its choice. We analyse the choice of regularization parameters for the 2-D adjoint tomography using synthetic tests.

Instead of the typically used (although criticized, e.g., Lévêque et al. (1993)) checkerboard test, we propose to carry out the tests with two different target models – simple smooth and complex realistic model. Tests with the simple model demonstrate the possibility of obtaining false small-scale structures. Contrarily, the tests with the complex target model reveal the possible resolving power of the present data set. The models shown are shown in Fig. 2:

- Model I: smooth model with small maximum amplitudes of the heterogeneity.

- Model II: complex model with pronounced small-scale structures and large maximum amplitudes.

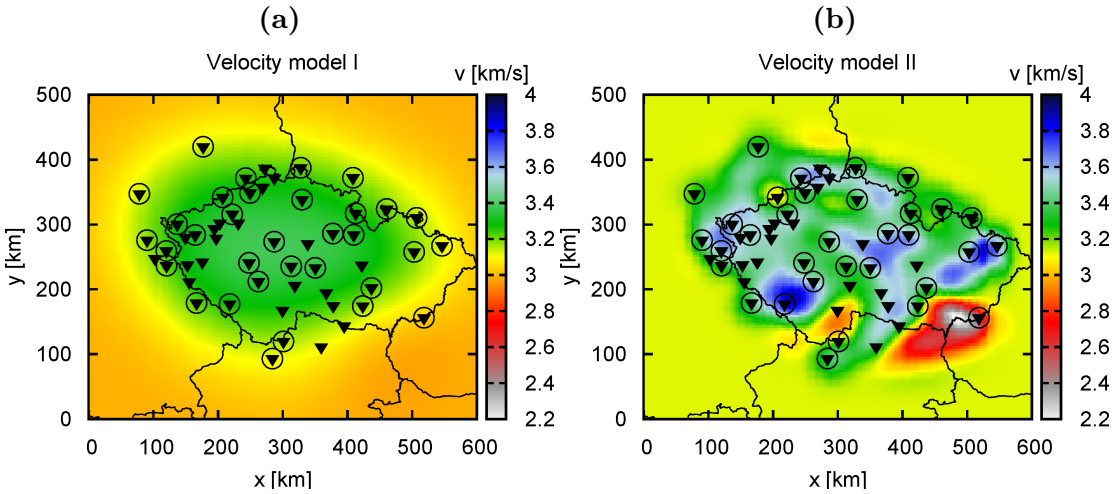

Figure 2: Velocity (target) models I (a) and II (b) for synthetic tests using 20 s data. Stations and sources are shown by inverted triangles and circles, respectively.

In the following tests, the synthetic data are modified assuming three values of the noise level specified in terms of the standard deviation. We benefit from having two independently obtained data sets of close frequency content, namely the 20 and 16 s Love-wave group traveltimes. Assuming that the differences between them are mostly due to the measurement error, their standard deviation is used as a reference "real" data noise for the synthetic tests σ_t. The other two levels are chosen for analysing the effect of smaller and larger data noise considering $1/3\sigma_t$ and $3/2\sigma_t$, respectively. The 'accurate' synthetic seismograms calculated for models shown in Fig. 2 are shifted by a value generated randomly from the corresponding Gaussian distribution. The waveforms themselves are not perturbed.

We smooth the calculated misfit gradients by means of convolution with a 2-D isotropic Gaussian function. We consider three widths (denoted as σ_x), 50, 100 and 150 km, representing different strengths of the smoothing. The smallest width corresponds to the wavelength of the 20 s data (or little less). This might be considered the natural choice because it prevents the smaller-than-wavelength structures without oversmoothing. The other two smoothing levels represent two different degrees of over-regularization.

The data coverage, that is the source-receiver configuration used in the synthetic tests, is the same as in the case of the real 20/16 s Love-wave data inversion and may be considered almost perfect for the inversion (see Fig. 2). The calculations were carried out using 2D adjoint version of software package SeisSol (Käser and Dumbser (2006) etc., see also http://www.seissol.org/).

Using the synthetic tests we investigate two effects on the convergence towards (or divergence from) a correct model: the effect of (i) noise level added to synthetics and (ii) spatial Gaussian smoothing of the gradient. To quantify model improvement, we define the model misfit as the L2 norm of the difference between the obtained model m_{n} at iteration n and target (i.e., true) model m_{targ}

normalized by the L2 norm of the initial model m_0: $\frac{||m_\mathrm{n}-m_\mathrm{targ}||}{||m_0||}\cdot 100\%$. Usually the curve has a local minimum. We denote the model corresponding to the minimum as the optimal model. Note that the model misfit is unknown in real applications because we do not know the true model.

The results for Test I and Test II are shown in the left and right column of Fig. 3, respectively. The individual rows show results for the three gradient smoothing levels σ_x (50, 100 and 150 km) with distinct colours and symbols. The decrease of data misfit (traveltime residual RMS) for the three noise levels is plotted in grey using the respective symbols and right axis.

Generally, during the first iteration steps of the inversions the structural model is improved at the longest wavelengths and both the model and the data misfit decrease considerably. During further iterations, the shorter wavelength structures of the model are revealed. The main difference between Test I and II is the number of iterations needed to achieve the optimum. When the target model contains smaller-scale structures, more iterations are needed in order to obtain the main features of the model and reach the optimum. At this point the performance of the inversion depends on the noise and smoothing levels. For the lowest noise level the model does not evolve considerably from the optimum. In case of the strong noise and weak smoothing, the model misfit grows with further iterations. For the higher noise level the increase of the model misfit starts earlier and is steeper. Nevertheless, the data misfit keeps decreasing, showing that the inversion starts explaining the noise in the data by new artificial structures in the model. With the increasing level of the gradient smoothing, the results stabilize in the optimum for more iterations. However, with application of the strongest smoothing of 150 km the recovered model is bound to contain only very long wavelength structures. This results in the higher value of the model misfit in the optimum in Test II as compared with other cases.

These tests show that in the presence of data noise a certain degree of over-regularization is necessary for obtaining a more stable result. However, in the case of very high data noise, it may be still insufficient and the inversion should be stopped after just a few iterations. For the real application (i.e. 20 s Love wave traveltimes) it follows that the iteration process should be stopped after 6 iterations considering Gaussian smoothing width $\sigma_x = 100$km. If the noise level σ_t was underestimated and the real model contains small-scale structures, the result should be stable without any profound artefacts. In case the real model does not contain small-scale structures and the data noise level is higher, the obtained model may suffer from false small-scale heterogeneities. However, the amplitudes of these anomalies should not be high and the artefacts should not be dominant features in the obtained models.

We also performed a similar test where we changed the position of stations. This test confirmed that these conclusions are independent on the source–receiver coverage.

We note that since the full 3-D adjoint inversions are computationally extremely expensive, the tests presented in this paper are feasible only in 2-D. We believe that they provide important insight into the method itself and reveal its main problems and limitations in general. From the presented numerical experiments, one may infer that the regularization (e.g., in the form of gradient smoothing) is recommended to be greater than the wavelength considered to pre-

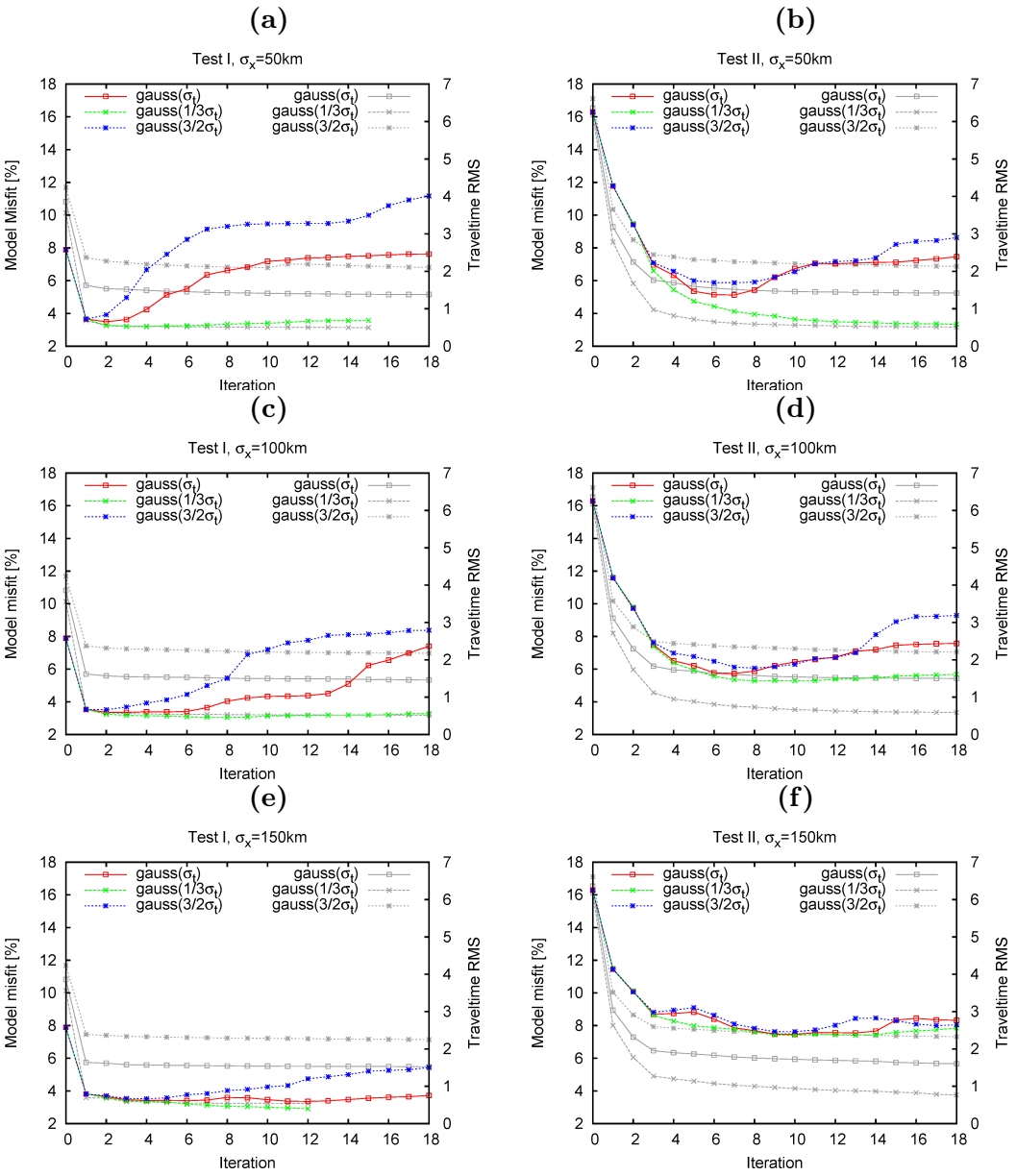

Figure 3: Results of Test I (left column) and Test II (right column). Colour curves and left vertical axis: convergence towards the target model represented by the model misfit. Grey curves and right vertical axis: data misfit in terms of traveltime residual RMS. Each row corresponds to a different level of the gradient smoothing: 50 km (top), 100 km (middle) and 150 km (bottom). The individual lines and symbols correspond to the different levels of noise applied to the synthetic data.

vent the bold structural artefacts. The proper number of iterations cannot be easily generalized because it strongly depends on the choice of the initial model. For applications similar to ours, the tests suggest that the number should be rather low ($\approx 5 - 10$). Otherwise, the model may be spoiled by the data noise artefacts even if the data coverage seems perfect.

3 Three-dimensional S-wave velocity model of the Bohemian Massif from Bayesian ambient noise tomography

Here we present the results of our ambient noise tomography into a 3D velocity model of the Bohemian Massif (see Fig. 4).

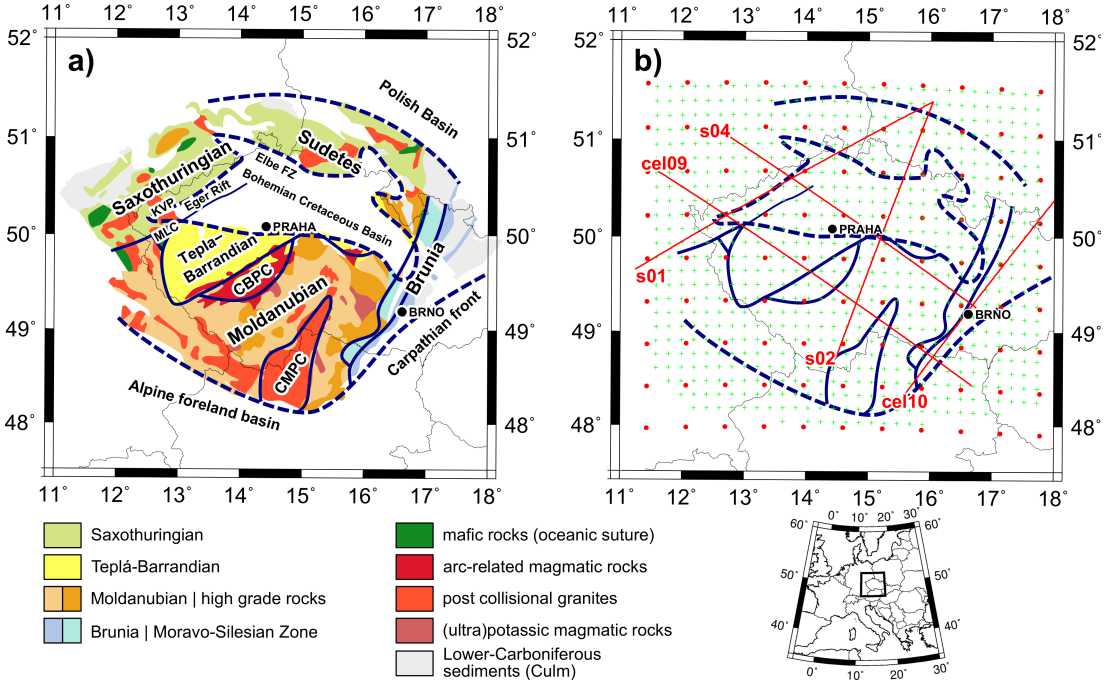

Figure 4: Map of the studied region: a) Main geologic structures of the Bohemian Massif modified after Franke (2000) and Schulmann et al. (2014). MLC – Mariánské Lázně Complex, CBPC – Central Bohemian Plutonic Complex, CMPC – Central Moldanubian Plutonic Complex, KVP – Karlovy Vary Pluton, FZ – fault zone. b) Distribution of points where the models are defined: Green pluses – data points where phase velocity dispersion maps are determined by 2D adjoint localization (first step). Red dots – model control points from which 3D velocity model is interpolated in the 3D inversion (second step). Selected seismic profiles measured during seismic experiments CELEBRATION 2000 (CEL09, CEL10) and SUDETES 2003 (S01, S02 and S04) across the studied region, are shown by red lines. Blue outlines show main geologic structures (solid – tectonic domains, dashed – post-Variscan sedimentary cover). Black thin outlines show state borders.

The stepping stone for our work are the ambient noise cross-correlation studies by Růžek et al. (2016) from which we adopted high quality inter-station dispersion

curves estimated independently for all components (transverse T, radial R and vertical Z) in period range 4–20 s.

The inversion is based on the traditional two-step approach. In the first step, we inverted the inter-station dispersion curves separately for the selected periods into a 2D regular grid (so-called phase velocity dispersion maps) using 2D adjoint method. For the second step, we performed the inversion of the dispersion maps into a 3D S-wave velocity model in a Bayesian framework.

The phase velocity dispersion maps are calculated for periods (4, 6, 8, 10, 12, 16, 20) s in the first stage and serve as input data in the second step of the inversion in which the Bayesian approach is applied. We extract dispersion curves in a selected 2D regular grid of data points (green pluses in Fig. 4b). The 3D velocity model is represented by a set of vertical 1D layered models on a regular horizontal grid of model control points (red dots in Fig. 4b). The spacing of the data and model control points is 16 km and 50 km, respectively. In each model control point, we assume 7 layers above a halfspace with interfaces at depths of 2, 4, 8, 12, 18, 24, and 32 km. Although the model is parametrized in 3D, the synthetic dispersion curves are calculated for computational reasons assuming 1D layered model at each data point. We employ the code VDISP which is based on a matrix method using Thomson-Haskell and Watson's matrices for Love and Rayleigh waves, respectively (Novotný (1999)). To obtain a 1D layered model for the synthetic dispersion curve calculation, the model is interpolated in each layer from the model control points into the data grid points by cubic spline interpolation.

The Bayesian inversion employs the PT algorithm with temperatures 1–50 to sample the posterior PDF. As the model prior information $p_{\text{prior}}(\mathbf{m})$ we use homogeneous PDF on a selected interval for all model parameters, in particular between 1 and 15 km/s. Another constraint on the model parameters is the requirement of a nonnegative velocity gradient with depth for each model control point. For simplicity, the data covariance matrix $\mathbf{C}_{\text{d}}$ is assumed to be diagonal with standard deviation corresponding to error of dispersion maps (see Section 3.1).

3.1 Phase velocity maps

Fig. 5 shows the inverted phase velocity dispersion maps for each period as obtained from the three components individually: Love (T) and both Rayleigh (R and Z). The perturbations in phase velocities are shown with respect to average values specified on the right side of each map.

We treat the dispersion curves for R and Z component as two independent datasets to get insight into the accuracy of the first part of the inversion. We use differences between both Rayleigh dispersion maps to estimate the error of the dispersion maps. The RMS of the differences ranges between $0.10 - 0.15$ s for different periods.

The phase-velocity dispersion maps were found to correlate well with known geology and are usually used for preliminary interpretation. In our dispersion maps (see Fig. 5), there is a high velocity structure in the southern part of the domain present in almost all maps, which may be related to the Moldanubian domain. Another stable high velocity anomaly, located in the center of the north-

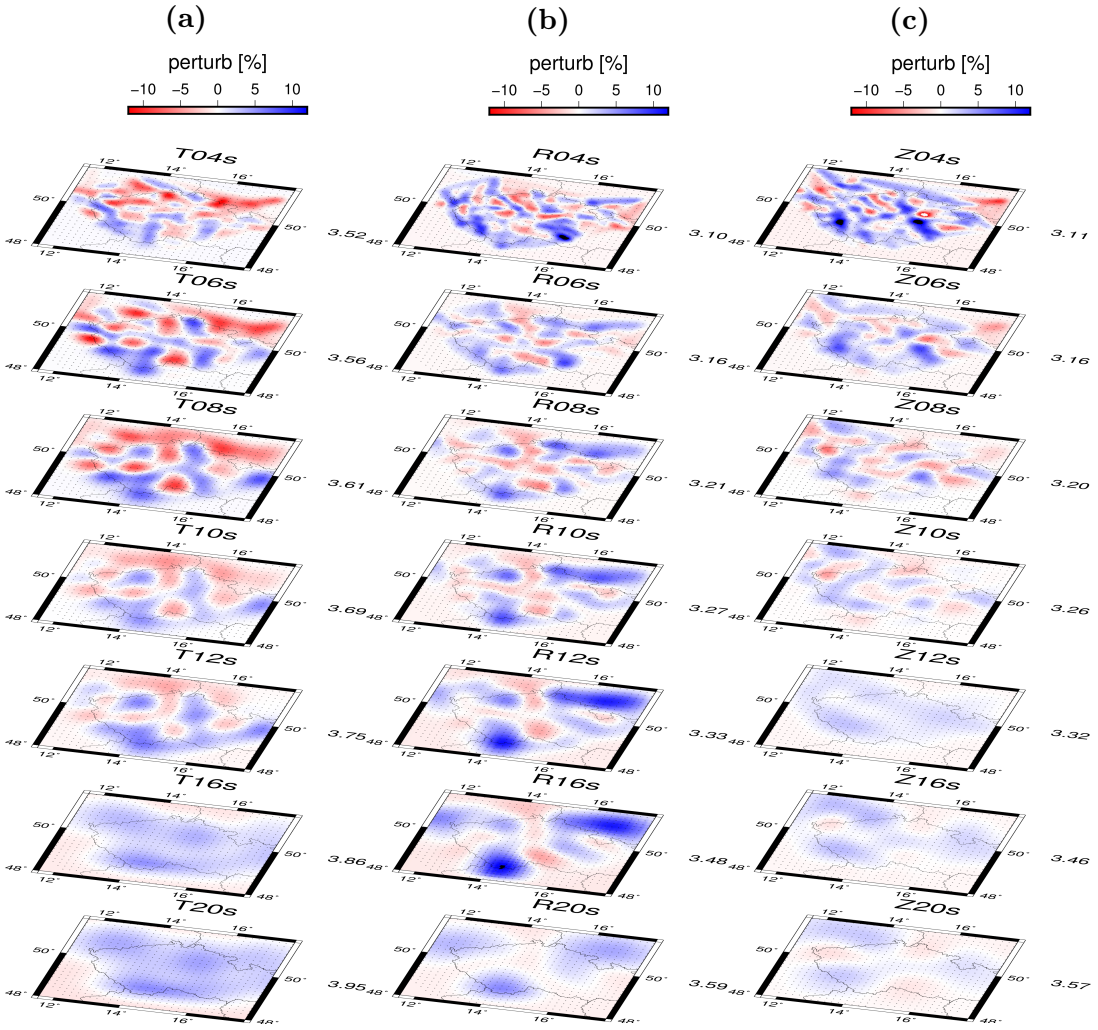

Figure 5: Phase velocity dispersion maps obtained by the 2D adjoint inversion for each period from all components: a) transverse T (i.e., Love wave), b) radial R c) vertical Z (both Rayleigh waves). The period increases from top to bottom (see legend). The model perturbations (color scale) are presented relative to mean phase velocity model, denoted for each map to the right in km/s.

west border of the Czech Republic is situated beneath the Eger Rift zone, where a high velocity body is usually found in the tomography (e.g., Grad et al. (2008)).

3.2 3D velocity models

The result of our Bayesian inversion consists of $>$ 1 million PDF samples (i.e., 3D models). To present the results, we display the mean model calculated from all models and the best model. The advantage of the mean model is that it presents only stable features. Therefore, the mean model is typically smoother than any single model drawn by the MC sampler. The best model is shown as a representative model to examine differences in properties between a single model and the averaged one.

Fig. 6 presents the depth-slices of the mean and the best 3D S-wave velocity model in terms of perturbations relative to the horizontally averaged model.

Both mean and best model share the most significant structures. The differences between them appear on smaller scales.

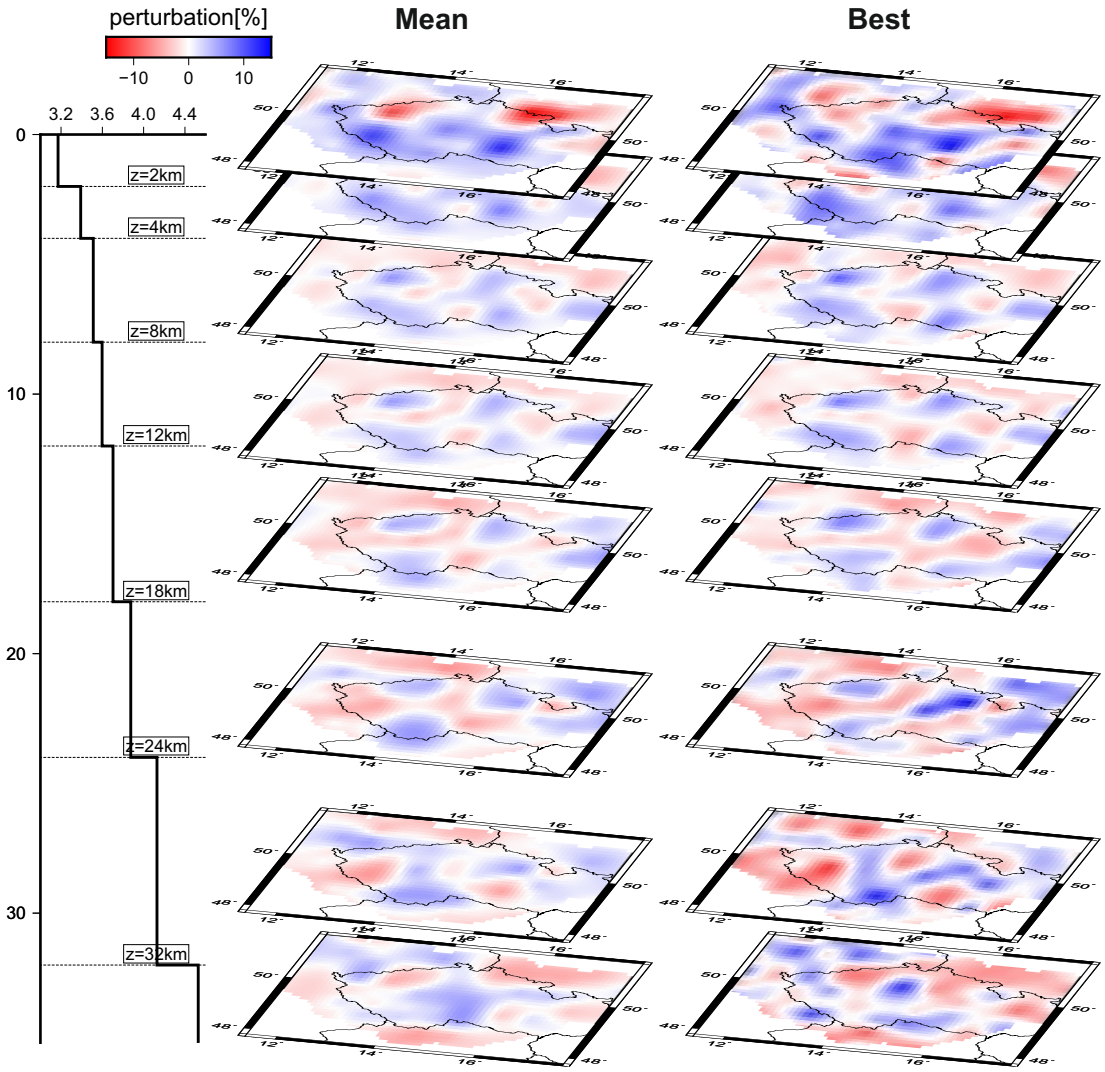

Figure 6: Depth slices through the mean (left) and best (right) S-wave velocity perturbations calculated as relative differences from horizontally averaged velocities (left panel). The areas with no station coverage are masked.

4 Discussion

4.1 Uncertainty of the 3D model

The greatest advantage of employing MC methods to solve the inverse problem lies in the plurality of models representing the solution. As an example, Fig. 7a shows vertical 1D models in a model control point located in the middle of our domain. From this example, we see that the best resolved part in the inversion lies at depths of 2–18 km. At greater depths, the variance in the S-wave velocities is very high. It also appears that the PDF of the S-wave velocities in deeper parts as well as v_p/v_s ratio have 2 local maxima. We ascribe this to the undersampling

of the PDF in the particular parameter domain. Also note that for model control points located at the boundaries of our domain, the overall uncertainty increases.

Uncertainty of the model along a profile can be estimated by standard deviation of the mean model (Fig. 7b right). In general, the lowest uncertainty (as indicated also by the 1D models in Fig. 7a) is achieved down to ∼20 km. However, the uncertainty changes also laterally along the profile (between 1–2% for the well resolved part). Alternatively, we visualize these changes via standard deviation of selected S-wave velocity isolines (Fig. 7b left).

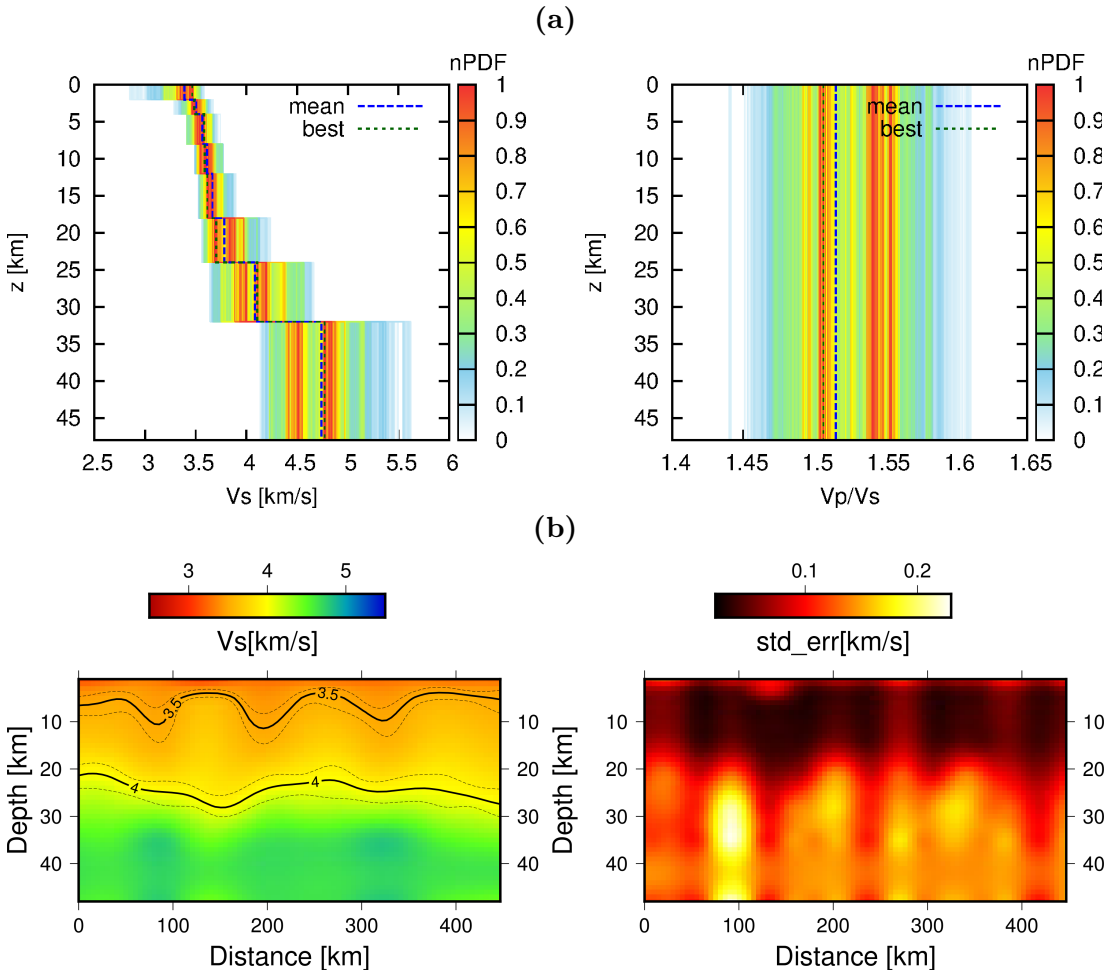

Figure 7: a) 1D vertical models in a selected model control point in the middle of the domain. Color palette shows nPDF – PDF normalized to its maximum (best model, see legend). b) 2D mean model and its variance interpolated along the CEL09 profile. Two velocity isolines are shown with their standard deviation.

We emphasize that we should be extremely cautious when interpreting the imaged structures below 25 km, where the model variance increases rapidly. In particular, our models are not suited for the search of the Moho. The following geologic interpretation should be confined to large-scale structures only. This limitation is a consequence of the method applied, namely: a) employment of surface wave data, which is inherently sensitive to the averaged (smoothed) structures both horizontally and vertically, making it impossible to obtain velocity interfaces; b) model parametrization – horizontal grid with relatively large (50 km)

spacing; and c) averaging of great amount of single models generated by the MC inversion which produces stable but smooth structures.

4.2 Geological interpretation of 3D S-wave velocity model

We solved the ambient noise tomography in the region of the Bohemian Massif, Variscan orogen with complex structure and history (see overview in Matte (2001); Franke (2000)). Due to its complex history and structure, the region of the Bohemian Massif has been subject to many seismologic studies starting from the 80s (see Novotný and Urban (1988)). Most of the recent crustal studies use active experiments along profiles, such as CELEBRATION 2000 and SUDETES 2003. The applied tomographic methods result in 2D vertical mainly P-wave velocity models (Hrubcová et al. (2005); Novotný (2012); Grad et al. (2008); Novotný et al. (2009); Hrubcová et al. (2010); Růžek et al. (2007))

Here, we correlate our 3D mean S-wave velocity model with known geology with the help of vertical cross-sections (Fig. 8), corresponding to selected profile measurements of active seismic experiments CELEBRATION 2000 (CEL09, CEL10) and SUDETES 2003 (S01, S02, S04), see also Fig. 4b).

The inferred 3D S-wave velocity model shows good correlation with main geologic domains of the Bohemian Massif. The Moldanubian domain is characterized by high S-wave velocities representing exposed middle/lower crustal material, except for a distinct anomaly located in its central part. Similarly to the Moldanubian, Brunia shows higher S-wave velocity anomalies. In contrast, the Teplá-Barrandian, Saxothuringian and Sudetes domains show lower S-wave velocities. In the Teplá-Barrandian domain which is composed of less consolidated upper crustal rocks, we have recovered a high velocity region with unclear geological interpretation resembling a promontory of the Moldanubian domain.

The most prominent high-velocity anomaly in the model is found beneath the Eger Rift. Moreover, some of the low S-wave velocity anomalies present in our model may correspond to large plutonic bodies, and the topmost low velocity structures correlate well with the sedimentary cover of the Bohemian Massif.

4.3 Comparison with local 1D models of Western Bohemia

Here we compare our model with 1D S-wave velocity models of Western Bohemia of other authors. We have extracted 1D model in a specific point (namely in station Nový Kostel, NKC) from our 3D model using cubic spline interpolation. This station is located in Western Bohemia region with periodic occurrence of earthquake swarms. Therefore, this area was subject to many tomographic invesigations, results of which are compared with ours (Novotný and Urban (1988); Novotný (1996); Málek et al. (2000); Růžek and Horálek (2013); Málek et al. (2005); Wilde-Piórko et al. (2005); Růžek et al. (2012); Kolínský et al. (2011), see Fig. 9).

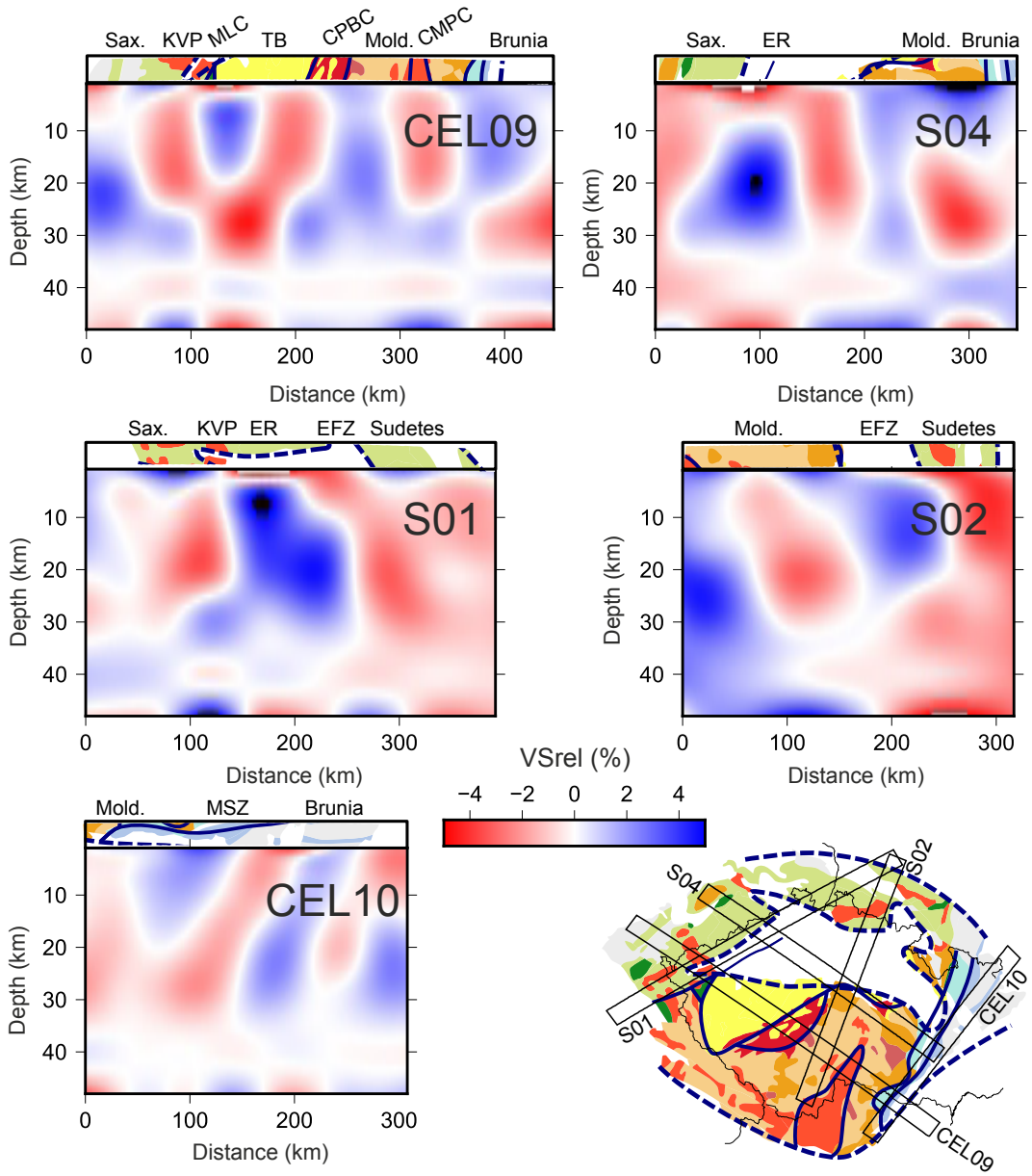

Figure 8: The S-wave velocity perturbations with respect to average model for each depth calculated from the mean model along the studied profiles. The main geologic structures are denoted on the top of each profile as indicated in the map in the inset panel. MLC – Mariánské Lázně Complex, CBPC – Central Bohemian Plutonic Complex, CMPC – Central Moldanubian Plutonic Complex, ER – Eger Rift, KVP – Karlovy Vary Pluton, EFZ – Elbe Fault Zone, Mold – Moldanubian, Sax – Saxothuringian, TB – Teplá-Barrandian, MSZ – Moravo-Silesian Zone.

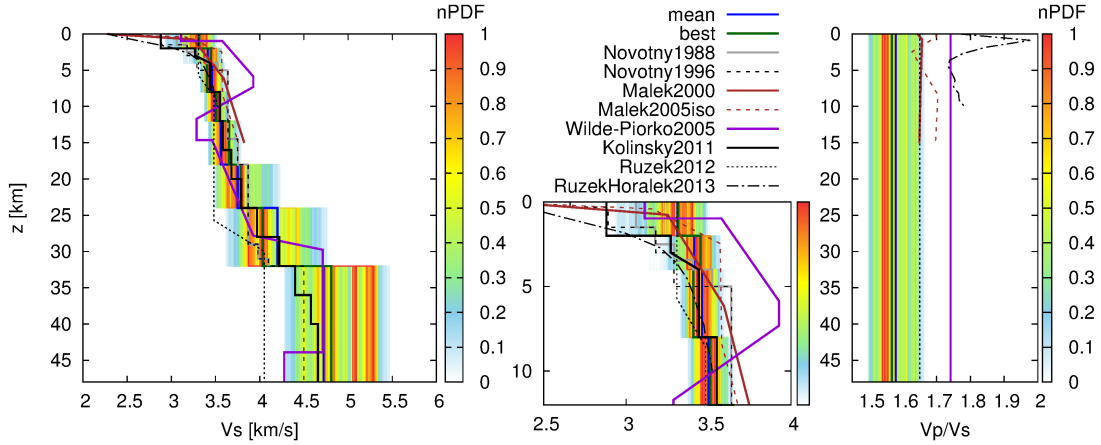

Figure 9: 1D model extracted from our 3D Bayesian model at station NKC (color coded): left – S-wave velocity model, right – v_p/v_s ratio. The resulting model samples are colored according to the normalized PDF value (nPDF), and the mean and best models are shown (see legend). The model is compared with 1D S-wave velocity models of Western Bohemia/NKC station of other authors (for more details see text). The inset in the middle is a zoom of the top 12km.

In general, all models are very close to our extracted 1D model mainly at depths 2-25 km. A larger discrepancy is in the subsurface part between our model and the shallow models (models reaching only to 10-15 km, i.e. Malek2000, Malek2005iso and RuzekHoralek2013, see also zoomed inset in the middle of Fig. 9), which is probably caused by low sensitivity and resolution of our data to these depths. Model by Wilde-Piórko et al. (2005) deviates from all other models in top 15 km, but its lower part (20-40 km) agrees with them.

Conclusions

We have performed the first 3D ambient noise tomography of the Bohemian Massif. The input data comprise of inter-station phase-velocity dispersion curves in range 4–20s prepared from ambient noise processing by Růžek et al. (2016). The inversion was carried out using two-step approach: in the first step, the dispersion curves were localized for each period into phase velocity dispersion maps and in the second step, these maps were inverted into a 3D S-wave velocity model.

To account for the finite-frequency effect, 2D adjoint inversion was utilized in the first step. Particular attention has been given to estimate the regularization parameters, such as width of the gradient smoothing function and number of iterations – subject not properly covered by literature despite having a crucial effect on the resulting model. To this aim, synthetic tests for the longest periods with two distinct target models were used, the first model was simple smooth model to demonstrate the emergence of model artifacts when insufficient smoothing is applied or too many iterations are performed. The second target model contains pronounced smaller-scale heterogeneities revealing the possibility to recover more-detailed structures in the resulting model. The synthetic data were modified by noise estimated from the differences between the 16s and 20s Love group

data. According to the tests, relatively large smoothing width (almost twice the wavelength) and rather small number of iterations (≈ 5) were found to be optimal. These values may appear to give too simple or over-regularized models. On the other hand, the resulting models contain weak but apparent smaller-scale heterogeneities which are, moreover, considered reliable assuming the estimated noise level.

The phase velocity dispersion maps were determined with the regularization parameters derived from the synthetic tests with the smoothing width scaled according to the respective wavelength. These maps serve as input data in the Bayesian inversion to obtain the 3D S-wave velocity model of the Bohemian Massif (and additionally depth-independent v_p/v_s ratio). The inversion was carried out employing Monte-Carlo sampler (in particular the so-called parallel tempering algorithm), combined with calculation of the dispersion curves in the layered model using matrix method. The main advantage of the Bayesian inversion is that the solution is represented not only by one 'best' model but by a large set of models, which are used to determine a mean model together with the uncertainty of the model parameters. As a result, more than one million model samples (i.e., 3D velocity models) following the posterior probability density function were obtained. From the estimated standard deviation we find that the best resolved part lies at depths 2-18 km ruling out determination of the Moho depth.

The mean model was correlated with known geologic structures of the Bohemian Massif. We must keep in mind that our method is able to recover only large-scale (smoothed) structures. The most prominent structure in the resulting model is a high velocity anomaly located beneath the Eger Rift, presently the most active area of the Bohemian Massif. The individual domains of the Bohemian Massif show higher velocity anomalies where high-grade metamorphism is expected (Moldanubian, Brunia), whereas other domains are characterized by rather low-velocity anomalies (Teplá-Barrandian, Saxothuringian and Sudetes). The uppermost part of the 3D velocity model shows good correlation between the low-velocity anomalies and sedimentary cover of the Bohemian Massif. Moreover, two significant anomalies with unknown geological interpretation were recovered: a low velocity anomaly in the Moldanubian domain and a high-velocity anomaly resembling a promontory of the Moldanubian into the Teplá-Barrandian domain under the Bohemian Cretaceous Basin.

Finally, our 1D S-wave velocity model of the Western Bohemia was compared with local models found by other authors, showing in general very good agreement in depths 2-18 km (i.e., where low variance of our model is obtained). This supports the results of our ambient noise tomography of the Bohemian Massif's crust as whole, which may give additional insight into its structure and development.

References

Fichtner, A., H.-P. Bunge, and H. Igel, The adjoint method in seismology: I. Theory, *Physics of the Earth and Planetary Interiors*, *157* **(1)**, 86–104, 2006.

Franke, W., The mid-European segment of the Variscides: tectonostratigraphic units, terrane boundaries and plate tectonic evolution, *Geological Society, London, Special Publications*, *179* **(1)**, 35–61, 2000.

Grad, M., A. Guterch, S. Mazur, G. R. Keller, A. Špičák, P. Hrubcová, and W. H. Geissler, Lithospheric structure of the Bohemian Massif and adjacent Variscan belt in central Europe based on profile S01 from the SUDETES 2003 experiment, *Journal of Geophysical Research: Solid Earth*, *113* **(B10)**, 2008, B10304.

Hrubcová, P., P. Środa, A. Špičák, A. Guterch, M. Grad, G. Keller, E. Brueckl, and H. Thybo, Crustal and uppermost mantle structure of the Bohemian Massif based on CELEBRATION 2000 data, *Journal of Geophysical Research: Solid Earth*, *110* **(B11)**, 2005, B11305.

Hrubcová, P., P. Środa, M. Grad, W. Geissler, A. Guterch, J. Vozár, E. Hegedűs, and S. . W. Group, From the Variscan to the Alpine Orogeny: crustal structure of the Bohemian Massif and the Western Carpathians in the light of the SUDETES 2003 seismic data, *Geophysical Journal International*, *183* **(2)**, 611–633, 2010.

Käser, M., and M. Dumbser, An arbitrary high-order Discontinuous Galerkin method for elastic waves on unstructured meshes – I. The two-dimensional isotropic case with external source terms, *Geophysical Journal International*, *166* **(2)**, 855–877, 2006.

Kolínský, P., J. Málek, and J. Brokešová, Shear wave crustal velocity model of the western Bohemian Massif from Love wave phase velocity dispersion, *Journal of seismology*, *15* **(1)**, 81–104, 2011.

Lévêque, J.-J., L. Rivera, and G. Wittlinger, On the use of the checker-board test to assess the resolution of tomographic inversions, *Geophysical Journal International*, *115* **(1)**, 313–318, 1993.

Liu, Q., and J. Tromp, Finite-Frequency Kernels Based on Adjoint Methods, *Bulletin of the Seismological Society of America*, *96* **(6)**, 2383–2397, 2006.

Luo, Y., and G. Schuster, Wave-equation traveltime inversion, *Geophysics*, *56* **(5)**, 645–653, 1991.

Málek, J., J. Horálek, and J. Janský, One-Dimensional qP-Wave Velocity Model of the Upper Crust for the West Bohemia/Vogtland Earthquake Swarm Region, *Studia Geophysica et Geodaetica*, *49* **(4)**, 501–524, Oct, 2005.

Málek, J., J. Janský, and J. Horálek, Layered Velocity Models of the Western Bohemia Region, *Studia Geophysica et Geodaetica*, *44* **(4)**, 475–490, Oct, 2000.

Matte, P., The Variscan collage and orogeny (480–290 Ma) and the tectonic definition of the Armorica microplate: a review, *Terra Nova*, *13* **(2)**, 122–128, 2001.

Novotný, M., Depth-Recursive Tomography of the Bohemian Massif at the CEL09 Transect—Part B: Interpretation, *Surveys in Geophysics*, *33* **(2)**, 243–273, 2012.

Novotný, M., Z. Skácelová, J. Mrlina, B. Mlčoch, and B. Růžek, Depth-recursive tomography along the Eger Rift using the S01 profile refraction data: tested at the KTB super drilling hole, structural interpretation supported by magnetic, gravity and petrophysical data, *Surveys in Geophysics*, *30* **(6)**, 561, Nov., 2009.

Novotný, O., and L. Urban, Seismic models of the Bohemian Massif and of some adjacent regions derived from deep seismic soundings and surface wave investigations: A review, *Induced Seismicity and Associated Phenomena*, , 227–249, 1988.

Novotný, O., A preliminary seismic model for the region of the West-Bohemian earthquake swarms, *Studia Geophysica et Geodaetica*, *40* **(4)**, 353–366, Oct, 1996.

Novotný, O., Seismic surface waves, http://geo.mff.cuni.cz/vyuka/Novotny-SeismicSurfaceWaves-ocr.pdf, 1999.

Růžek, B., P. Hrubcová, M. Novotný, A. Špičák, and O. Karousová, Inversion of travel times obtained during active seismic refraction experiments CELEBRATION 2000, ALP 2002 and SUDETES 2003, *Studia Geophysica et Geodaetica*, *51* **(1)**, 141–164, 2007.

Růžek, B., J. Plomerová, and V. Babuška, Joint inversion of teleseismic P waveforms and surface-wave group velocities from ambient seismic noise in the Bohemian Massif, *Studia Geophysica et Geodaetica*, *56* **(1)**, 107–140, 2012.

Růžek, B., L. Valentová, and F. Gallovič, Significance of Geological Units of the Bohemian Massif, Czech Republic, as Seen by Ambient Noise Interferometry, *Pure and Applied Geophysics*, *173* **(5)**, 1663–1682, 2016.

Růžek, B., and J. Horálek, Three-dimensional seismic velocity model of the West Bohemia/Vogtland seismoactive region, *Geophysical Journal International*, *195* **(2)**, 1251–1266, 2013.

Sambridge, M., A Parallel Tempering algorithm for probabilistic sampling and multimodal optimization, *Geophysical Journal International*, *196* **(1)**, 357, 2014.

Schulmann, K., O. Lexa, V. Janoušek, J. M. Lardeaux, and J. B. Edel, Anatomy of a diffuse cryptic suture zone: An example from the Bohemian Massif, European Variscides, *Geology*, *42* **(4)**, 275–278, 2014.

Tarantola, A., *Inverse problem theory and methods for model parameter estimation*. SIAM, 2005.

Tromp, J., C. Tape, and Q. Liu, Seismic tomography, adjoint methods, time reversal and banana-doughnut kernels, *Geophysical Journal International*, *160* **(1)**, 195–216, 2005.

Wilde-Piórko, M., J. Saul, and M. Grad, Differences in the Crustal and Uppermost Mantle Structure of the Bohemian Massif from Teleseismic Receiver Functions, *Studia Geophysica et Geodaetica*, *49* **(1)**, 85–107, 2005.

Author's publications

Růžek, B., L. Valentová, and F. Gallovič, Significance of Geological Units of the Bohemian Massif, Czech Republic, as Seen by Ambient Noise Interferometry, *Pure and Applied Geophysics*, *173* **(5)**, 1663–1682, 2016.

Valentová, L., F. Gallovič, B. Růžek, J. de laPuente, and P. Moczo, Choice of regularization in adjoint tomography based on two-dimensional synthetic tests, *Geophysical Journal International*, *202* **(2)**, 787–799, 2015.

Valentová, L., F. Gallovič, and P. Maierová, Three-dimensional S-wave velocity model of the Bohemian Massif from Bayesian ambient noise tomography, *Tectonophysics*, *717* **(C)**, 484 – 498, 2017.